Aalborg Universitet

AALBORG UNIVERSITY

Transfer function and near-field detection of evanescent waves

Radko, Ilya; Bozhevolnyi, Sergey; Gregersen, Niels

[Link to publication from Aalborg University](#)

Transfer function and near-field detection of evanescent waves

Ilya P. Radko, Sergey I. Bozhevolnyi, and Niels Gregersen

We consider characterization of a near-field optical probe in terms of detection efficiency of different spatial frequencies associated with propagating and evanescent field components. The former are both detected with and radiated from an etched single-mode fiber tip, showing reciprocity of collection and illumination modes. Making use of a collection near-field microscope with a similar fiber tip illuminated by an evanescent field, we measure the collected power as a function of the field spatial frequency in different polarization configurations. Considering a two-dimensional probe configuration, numerical simulations of detection efficiency based on the eigenmode expansion technique are carried out for different tip apex angles. The detection roll-off for high spatial frequencies observed in the experiment and obtained during the simulations is fitted using a simple expression for the transfer function, which is derived by introducing an effective point of (dipolelike) detection inside the probe tip. It is found to be possible to fit reasonably well both the experimental and the simulation data for evanescent field components, implying that the developed approximation of the near-field transfer function can serve as a simple, rational, and sufficiently reliable means of fiber probe characterization.   © 2006 Optical Society of America

OCIS codes: 110.2990, 110.4850, 180.5810.

1. Introduction

A transfer function is an important notion in any imaging technique, which allows one to relate an image and an object presuming, of course, that the process of image formation is linear. Most often, the intensity distribution of light in an image is related to the intensity distribution at the corresponding object plane. It determines the spatial resolution of an imaging instrument and also allows for consideration of the inverse problem. In conventional (far-field) microscopy, knowledge of the optical transfer function makes it possible to reconstruct the object structure from a recorded image.[1] In scanning near-field optical microscopy (SNOM), multiple scattering in the probe–sample system usually takes place. Therefore one should consider the self-consistent field, which greatly complicates the situation. It has

been shown,[2] however, that the probe–sample interaction is negligible in photon tunneling (or, in general, collection) SNOM (PT-SNOM) with uncoated fiber probes. For this reason the transfer function is mainly discussed in relation to the collection SNOM.

The notion of a transfer function in near-field microscopy is not a new one. It had been implicitly assumed already in 1993 by Tsai *et al.*[3] and by Meixner *et al.*[4] in their works with experimental determination of spatial resolution of the PT-SNOM. Theoretical investigations, showing that the signal detected in the PT-SNOM is proportional to the square modulus of the electric near field[5] and suggesting accounting for a finite size of the probe by means of a transfer function,[6] resulted in wide usage of the intensity transfer function (ITF) while treating the experimental results.[7–11] This ITF relates the Fourier transform (FT) of a near-field optical image to the FT of a corresponding intensity distribution. Nevertheless, the very existence of such a transfer function has been questioned judged on the basis of numerical results,[12] experimentally in the context of probe characterization[13] and theoretically[14] using treatment of image formation developed previously by Greffet and Carminati.[15] Moreover, it has been shown that the notion of ITF can be used in only some particular cases, i.e., using

several approximations.[14] Instead, an amplitude-coupling function (ACF) has been suggested for the characterization of the collection SNOM. On the other hand, it is rather difficult to measure both the magnitude and the phase of the ACF for a given SNOM arrangement, since it requires the use of phase detection techniques. From the point of view of SNOM resolution, the most important characteristic is the ACF magnitude or, more precisely, its decay for high spatial frequencies corresponding to evanescent field components. It is this decay that (along with the noise level) determines the spatial resolution attainable with the SNOM. For this reason, we are concerned in this paper with the measurements and simulations of the ACF magnitude, especially in the domain of evanescent field components.

The paper is organized as follows. In Section 2 we review the main formulas, explaining the image formation process, and introduce a simple approximation for the ACF based on the idea of point-dipole detection by an extremity of a SNOM fiber tip.[5] Then, in Section 3, we present our measurements of the ACF magnitude in different configurations, detecting far- and near-field wave components. Section 4 presents the results of numerical simulations of the coupling efficiency in two-dimensional (2D) geometry. It has been argued elsewhere[16,17] that the use of 2D simulations simplifies considerably the computational effort without loss of the essential features of the SNOM imaging process. In Section 5 we discuss the results obtained utilizing the suggested approximation for the probe ACF. In Section 6, we offer our conclusions.

2. Background

Let us consider image formation in the collection SNOM, in which a fiber tip scanned near an illuminated sample surface is used to probe an optical field formed at the surface (Fig. 1). This field is scattered by the tip, also inside the fiber tip itself, coupling thereby to fiber modes that are formed far from the probe tip and propagating toward the other end of the fiber to be detected.[14,15] To relate the fiber mode amplitudes to the plane-wave components of the probed field, it is convenient to make a plane-wave Fourier decomposition of the incident electric field $\mathbf{E}(\mathbf{r}_\parallel, z)$ in the plane $z = 0$ parallel to the surface and passing through the probe tip end:

$$\mathbf{E}(\mathbf{r}_\parallel, 0) = \frac{1}{4\pi^2} \int \int \mathbf{F}(\mathbf{k}_\parallel, 0)\exp(i\mathbf{k}_\parallel \cdot \mathbf{r}_\parallel)\mathrm{d}\mathbf{k}_\parallel, \quad (1)$$

where $\mathbf{r}_\parallel = (x, y)$ and $z = 0$ are coordinates of the tip end, $\mathbf{k}_\parallel = (k_x, k_y)$ is the in-plane projection of the wave vector, and $\mathbf{F}(\mathbf{k}_\parallel, z)$ is the vector amplitude of the corresponding plane-wave component of the incident field. Since, as already mentioned, the multiple probe–sample scattering can be disregarded in the collection SNOM, the field described by Eq. (1) is considered to be
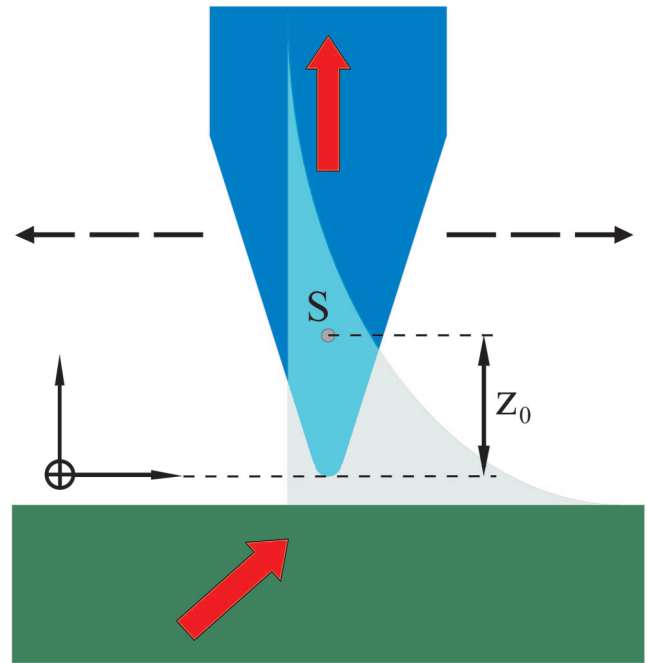

Fig. 1. (Color online) Coordinate system and schematics of near-field detection by a fiber tip. Point S situated at distance z_0 from the tip extremity represents an effective detection point at which coupling of the incident field to the fiber mode is considered to take place.

the only one that makes a contribution to the detected signal. To relate the plane-wave components to the fiber mode amplitudes excited in the probe fiber, we further assume that the fiber used is single mode and weakly guiding, oriented perpendicular to the surface, and terminated with a probe tip possessing axial symmetry. Note that, for weakly guiding fibers (having a very small index difference between the fiber core and its cladding), the guided modes represent approximately transverse-electromagnetic (TEM) waves. Thus, in the considered case, any propagating field distribution can be decomposed into two orthogonally polarized fiber modes, whose amplitudes we shall denote as A_x and A_y. It should be mentioned in passing that the origin of the probed field [see Eq. (1)] is irrelevant in this consideration and that the sample surface serves merely as a reference plane surface sustaining the field with high spatial frequencies (i.e., evanescent wave components).

We can further reason that, in the case of s-polarized illumination, one should expect to find, for symmetry reasons, only a y-polarized component of the field in the above plane-wave decomposition and a similarly polarized fiber mode (Fig. 1). In the case of p polarization, one should, however, expect to find x- and z-polarized field components in the above decomposition. Again using symmetry considerations, it transpires that both components can contribute only to the x component of the fiber mode, since the z-polarized field component having the symmetric orientation with respect to the probe axis does propagate along the x axis. Taking these arguments into
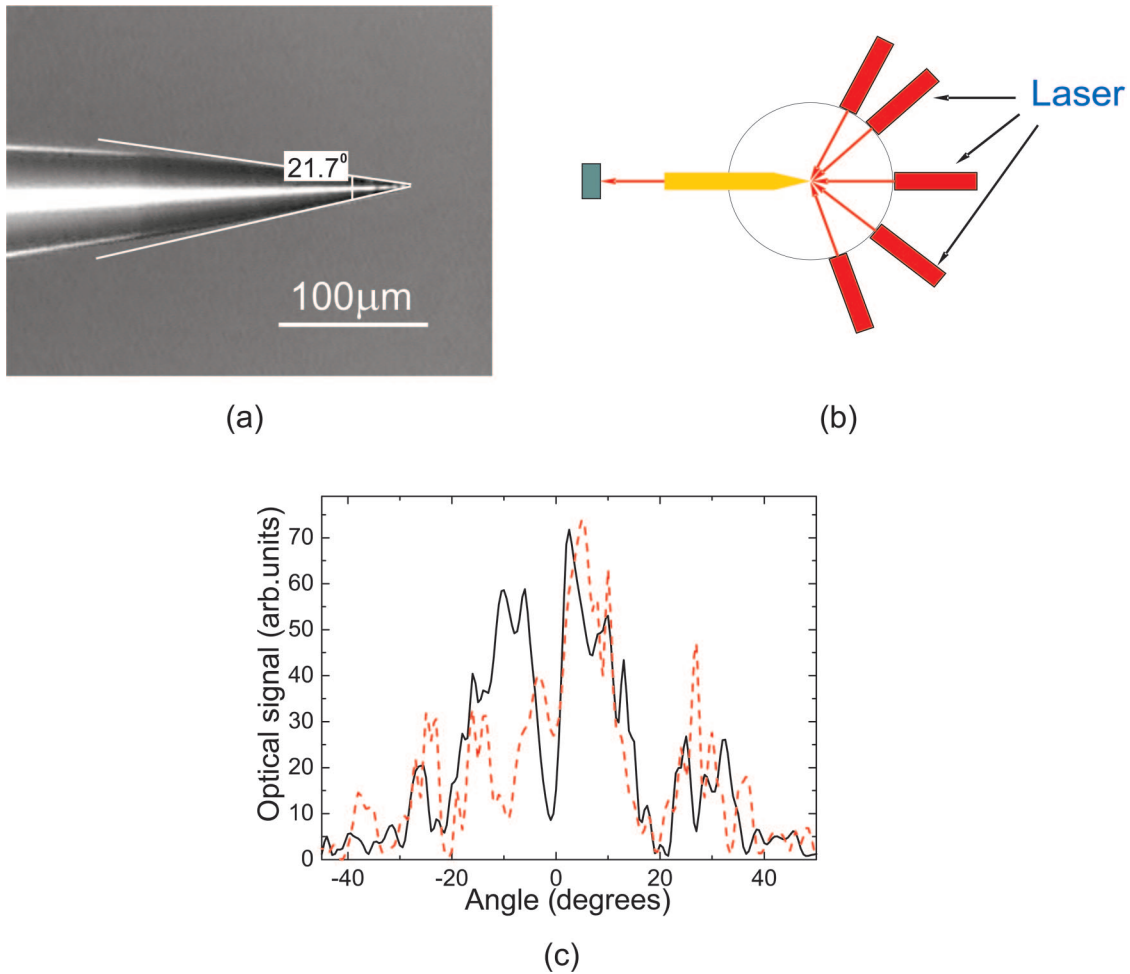
Fig. 2. (Color online) (a) Fiber tip used in both far- and near-field measurements. (b) Experimental setup for the far-field measurements in collection mode along with (c) the results obtained for s (solid curve) and p polarization (dashed curve).

account we can express the mode amplitudes of a (single-mode) fiber as follows:

$$A_y(\mathbf{r}_\parallel) = \frac{1}{4\pi^2} \iint H_{yy}(\mathbf{k}_\parallel) F_y(\mathbf{k}_\parallel, \; 0) \exp(i\mathbf{k}_\parallel \cdot \mathbf{r}_\parallel) d\mathbf{k}_\parallel,$$

$$A_x(\mathbf{r}_\parallel) = \frac{1}{4\pi^2} \iint [H_{xx}(\mathbf{k}_\parallel) F_x(\mathbf{k}_\parallel, \; 0)$$
$$+ H_{xz}(\mathbf{k}_\parallel) F_z(\mathbf{k}_\parallel, \; 0)] \exp(i\mathbf{k}_\parallel \cdot \mathbf{r}_\parallel) d\mathbf{k}_\parallel, \quad (2)$$

where $H_{ij}(\mathbf{k}_\parallel)$ are the coupling coefficients that account for the contribution of the jth plane-wave component to the ith component of the fiber mode field. The matrix $\mathbf{H}$ composed of (amplitude-coupling) coefficients H_{ij} plays a role in the ACF, which represents the coupling efficiency for various spatial frequencies and, for example, determines the maximum attainable spatial resolution when imaging with the SNOM.

The exact form of an ACF depends, in general, on the probe characteristics (shape, refractive index composition, etc.) and can be rather cumbersome to determine.[15] It is clear, however, that the ACF mag-

nitude should decrease for high spatial frequencies. This is probably the most important feature of the ACF that should be present in any ACF approximation. We suggest a description of the ACF using the following model. Let us view the detection process as radiation scattering by a pointlike dipole situated inside the tip (point S in Fig. 1) at the distance z_0 from the tip extremity. Its scattering efficiency (into a given fiber mode) depends only on the corresponding component of the (incident) field at the site of the dipole:

$$A_y(\mathbf{r}_\parallel) = c_\parallel E_y(\mathbf{r}_\parallel, z_0),$$
$$A_x(\mathbf{r}_\parallel) = c_\parallel E_x(\mathbf{r}_\parallel, z_0) + c_\perp E_z(\mathbf{r}_\parallel, z_0). \quad (3)$$

Making decompositions in the field expressions above that are similar to that in Eq. (1) but at the plane $z = z_0$ containing the detection point S, one obtains

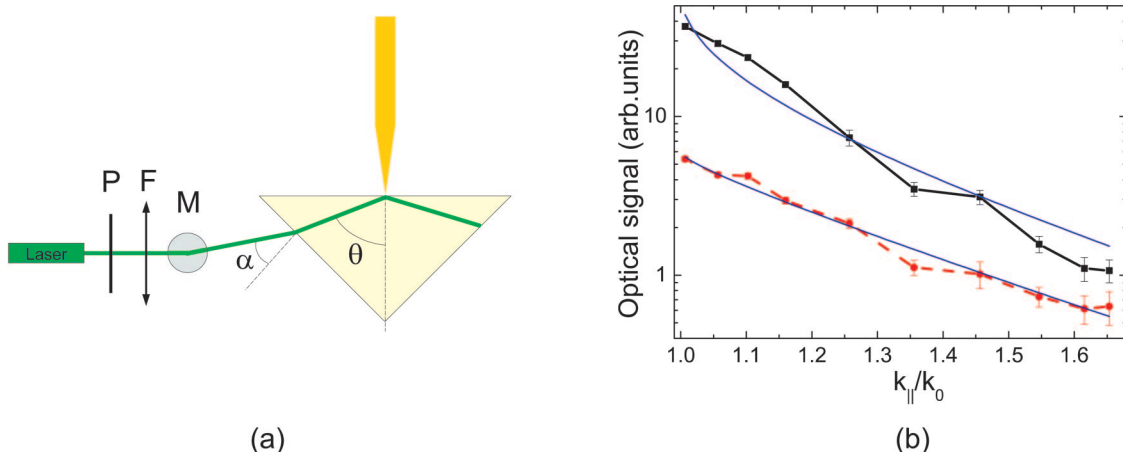$$H_{yy}(\mathbf{k}_\parallel) F_y(\mathbf{k}_\parallel, \; 0) = c_\parallel F_y(\mathbf{k}_\parallel, z_0),$$

$$H_{xx}(\mathbf{k}_\parallel) F_x(\mathbf{k}_\parallel, \; 0) + H_{xz}(\mathbf{k}_\parallel) F_z(\mathbf{k}_\parallel, \; 0) = c_\parallel F_x(\mathbf{k}_\parallel, z_0)$$
$$+ c_\perp F_z(\mathbf{k}_\parallel, z_0). \quad (4)$$

Fig. 3. (Color online) (a) Schematics of a fiber tip used in illumination mode and the light distribution in front of the fiber tip produced by a CCD camera. (b) Far-field signal dependencies measured in illumination mode for s (solid curve) and p polarization (dashed curve).

Finally, taking into account that $H_{xx} = H_{yy}$ and considering only evanescent field components, the following relations for the ACF components can be written:

$$H_{xx}(k_{\parallel} \geq k_0) = H_{yy}(k_{\parallel} \geq k_0) = c_{\parallel} \exp\left(-z_0\sqrt{k_{\parallel}^2 - k_0^2}\right),$$

$$H_{xz}(k_{\parallel} \geq k_0) = c_{\perp} \exp\left(-z_0\sqrt{k_{\parallel}^2 - k_0^2}\right), \quad (5)$$

where k_0 is the wavenumber in air, i.e., $k_0 = 2\pi/\lambda$ and λ is the light wavelength in air. The obtained (approximate) ACF expressions [Eqs. (2) and (5)] represent the main result of our consideration. This approximation being simple and rather transparent also preserves the vectorial character of the ACF[14,15] and contains the detection roll-off for high spatial frequencies. We demonstrate below that it can also be fitted reasonably well to approximate both experimental and simulation data.

3. Experimental Results

A. Far-Field Measurements

In this part of the experiment, first, a laser ($\lambda = 633$ nm, $P \sim 1.5$ mW) beam having s or p polarization (the electric field is parallel or perpendicular to the plane of incidence) illuminated the tip of a fiber probe under investigation [Fig. 2(a)] under different angles of incidence [Fig. 2(b)]. The power of coupled radiation was registered at the output end of the fiber by a photodetector. The probe was produced from a single-mode optical fiber (the cutoff wavelength was $\sim$780 nm). On the scale of the probe tip apex, where the coupling actually takes place, the (Gaussian) laser beam can be considered as a plane wave, so the detected signal should be proportional to the squared magnitude of the corresponding ACF component, at least in the case of s polarization. Measurements for both polarizations showed that the detected signal oscillates strongly with the spatial frequency for relatively small angles of incidence ($<40°$) and rapidly

Fig. 4. (Color online) (a) Schematics of near-field measurements in collection mode: P, polarizer; F, focusing lens; M, rotational mirror to change angle α and thereby angle θ, which was kept larger than the critical angle of total internal reflection. (b) Signal dependencies obtained for s (solid curve) and p polarization (dashed curve). Fitting shown by thin solid lines is made for each curve as explained in Section 5.
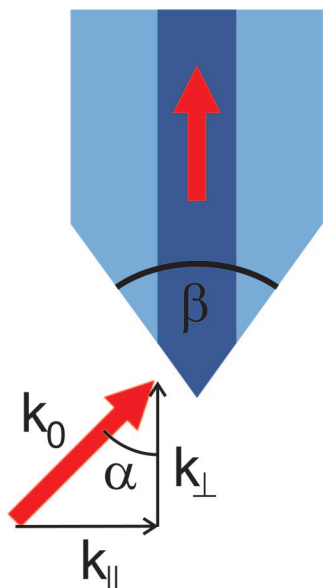
Fig. 5. (Color online) Two-dimensional geometry used in numerical simulations of the coupling process. The following parameters have been used in the simulations: $\lambda = 633$ nm, core diameter of 4 μm, core index of 1.459, cladding index of 1.457.

decreases for large angles [Fig. 2(c)]. We consider strong oscillations as the manifestation of Mie (shape) resonances that can be excited in an uncoated fiber tip by propagating waves. Perhaps a better understanding of such behavior of the registered signal can be perceived considering the image of light intensity distribution obtained with a CCD camera placed in front of the probe, with the laser radiation being coupled in the fiber from another end [Fig 3(a)]. Here, one should expect to find the reciprocity between the illumination and collection SNOM modes.[15] The experimental dependence of the detected throughput illumination on the angle of detection is shown in Fig. 3(b) and is produced in the setup, similar to that shown in Fig. 2(b), with the laser and the photodetector being exchanged. A similar dependence can be obtained by making a (properly chosen) cross section of the image from Fig. 3(a). The fact that this cross section should be displaced away from the fiber axis can be explained by a slight displacement of the rotational plane of the photodetector (or the laser) with respect to the fiber probe axis.

B. Near-Field Measurements

The near-field measurements provided more accurate and straightforward data, allowing us to characterize the probe detection efficiency in the domain of evanescent field components. Our experimental setup is schematically shown in Fig. 4(a). A SNOM apparatus was used to scan a small area of the prism surface illuminated from the side of the prism with a slightly focused laser beam ($\lambda = 543.5$ nm, $P \sim 1.5$ mW) being totally internally reflected. By changing the incident angle θ and using a high-refractive-index prism ($n = 1.73$), it was possible to realize the illumination with spatial frequencies

varying from 1.0 up to 1.67, when being expressed in a normalized form, i.e., $k_\parallel/k_0 = n \sin \theta$. The results obtained for s and p polarizations are shown in Fig. 4(b) by bold solid and dashed curves, respectively. To separate the graphs, the data for s polarization have been moved up by a factor of 3. Also in this case, we can reason that the measured signal dependencies are directly related to the squared ACF magnitudes.

4. Numerical Simulations

We also calculated the electromagnetic field distribution around the fiber tip subject to the illumination from below. For an incoming plane wave with a specific value of $k_\parallel = |\mathbf{k}_\parallel|$, we determined the amount of power coupled to the fundamental fiber mode. Varying the value of $k_\parallel$, we obtained the (spatial-) frequency-dependent transmission, which is again related to the squared magnitudes of the ACF components.

Because full vectorial calculations of light scattering on three-dimensional (3D) nanoscale structures are computationally demanding, we have considered a 2D fiber with uniformity along one lateral axis. The geometry of the refractive index profile is depicted in Fig. 5. The core and cladding indices of the fiber are 1.459 and 1.457, respectively; the core diameter is 4 μm, and, to increase computation speed, a reduced cladding diameter of 20 μm was chosen. The opening angles were varied from 10° to 70°.

The simulation method used to calculate the electromagnetic field was the eigenmode expansion technique. In this procedure, the refractive index geometry is divided into layers of a uniform refractive index profile along a propagation axis, here chosen as the Z axis. Eigenmode and propagation constants are calculated in each layer, and the fields at each side of a layer interface are connected using the transfer-matrix formalism. The general method is described in Ref. 18. For the eigenmode computation, a plane-wave basis was chosen with a discrete number of plane waves; further details of the eigenmode determination are given in Ref. 19.

The graded part of the fiber tip was modeled using a discrete step-index profile, and the entire geometry was enclosed in a box with periodic boundary conditions. The number of steps in the step-index profile and plane waves in the discrete basis as well as the box size were increased until the transfer function converged. The resulting transmissions for two polarizations of the incident field and for various opening angles are depicted in Fig. 6 as a function of normalized spatial frequency. It is seen that, for propagating field components, the transmission exhibits strong oscillations, whereas it rapidly and monotonously decreases for high spatial frequencies corresponding to evanescent field components. This behavior is qualitatively similar to that observed in the experiment reported above.

5. Discussion

First, we should notice a resemblance in the angular dependencies of the signal detected by the
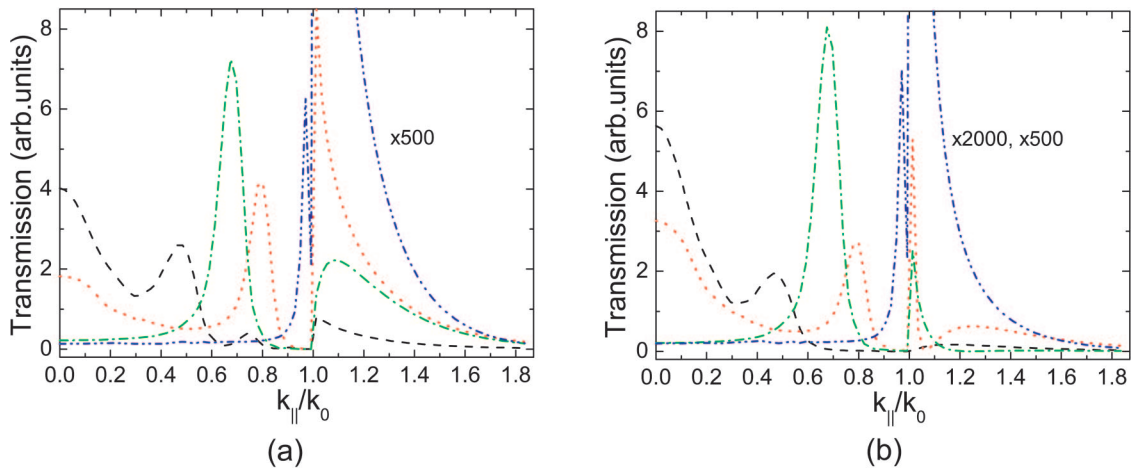
Fig. 6. (Color online) Numerical results for the coupled (transmitted through the fiber) electric field amplitude obtained for (a) s and (b) p polarization and for different apex angles β (Fig. 5): 10° (dashed curve), 30° (dotted curve), 50° (dashed–dotted curve), and 70° (dashed–dotted–dotted curve). Note that in the evanescent field domain ($k_\parallel/k_0 > 1$) the data are multiplied by a factor of 500 for s polarization (all angles) and p polarization (for 10° and 30°) and by a factor of 2000 for p polarization and for 50° and 70°.

SNOM probe [Fig. 2(c)] and simulated (for the propagating field components) transmission (Fig. 6): Both are of oscillatory behavior featuring maxima and minima. In the domain of the evanescent field components ($k_\parallel/k_0 > 1$), it transpires from both experimental and theoretical results that the ACF rolloff is well pronounced, implying the possibility of using our approximation [Eqs. (5)]. In the case of s polarization (containing evanescent wave components), the first formula in Eqs. (5) can be applied directly. For p polarization, however, one has to consider two components, parallel and perpendicular to the surface plane ($\mathbf{E}_p = \mathbf{E}_\parallel + \mathbf{E}_\perp$), whose detection efficiencies related to the coefficients H_{xx} and H_{xz} are different. When deriving an expression for the ACF in this case, one should take into account the ratio $E_z/E_x = ik_\parallel/(k_\parallel{}^2 - k_0{}^2)^{1/2}$, which can be obtained easily from the Gauss law: div $\mathbf{E} = 0$. Furthermore, one should expect that the coupling coefficients (H_{xx} and H_{xz}) are different not only in magnitude but also in phase, arriving at the following expressions:

$$H_s(k_\parallel \geq k_0) = A \exp\left(-z_0\sqrt{k_\parallel{}^2 - k_0{}^2}\right),$$

$$H_p(k_\parallel \geq k_0) = B\sqrt{1 - (k_0/k_\parallel)^2}\ \exp\left(-z_0\sqrt{k_\parallel{}^2 - k_0{}^2}\right) + C\exp(i\varphi)\exp\left(-z_0\sqrt{k_\parallel{}^2 - k_0{}^2}\right). \quad (6)$$

We fitted the experimental signal dependencies measured for the illumination with evanescent field components with the squared functions from Eqs. (6), since the experimental results represent power measurements. Considering s and p polarizations, we have obtained the following fitting parameters: $z_0 \approx 140$ nm, $B/C \approx 1.2$, and $\varphi \approx \pi$. It is seen that the correspondence between experimental and approximated dependencies is reasonably good [Fig. 4(b)] and that the fitting parameters are consistent with the observations reported previously. Thus a good

correspondence between calculated field intensity distributions at a 100 nm distance over a rough nanostructured surface and near-field intensity distributions measured with the tip–surface distance of ∼5 nm was found,[20] suggesting that the effective detection point was located inside a fiber tip at a distance of ∼100 nm from its extremity. Measurements and simulations of field phase and amplitude distributions over diffraction gratings also supported the concept of effective detection occurring at some distance from the tip extremity.[21] In addition, it has been experimentally demonstrated that the SNOM detection introduces polarization filtering, so that the field component perpendicular to the surface is detected (with an uncoated fiber tip) less efficiently than the parallel component.[22] In our case, the polar-

Table 1. Fitting Parameters for Different Tip Apex Angles[a]

Tip Apex Angle (deg)	z_0 (nm)	φ	A	B	B/C
10	(138 ± 20)	(1.01 ± 0.03)π	0.14	0.19	24.8
20	(141 ± 20)	(1.00 ± 0.03)π	0.25	0.29	12.1
30	(151 ± 35)	(1.05 ± 0.03)π	0.24	0.82	3.0
40	(146 ± 35)	(1.19 ± 0.05)π	0.31	0.50	2.1
50	(155 ± 20)	(1.02 ± 0.03)π	0.39	0.51	1.7
60	(160 ± 35)	(1.12 ± 0.04)π	0.49	0.47	1.2
70	(210 ± 20)	(1.20 ± 0.05)π	1.02	1.58	1.4

[a]Parameters found from fitting the data obtained in the numerical simulations of detection efficiency for different spatial frequencies: distance z_0, position of the effective detection point of a near-field probe; φ, phase difference between two field components in the p-polarized incident light; A, contribution coefficient from the incident field of the s-polarized light to the coupled field; B, contribution coefficient from the in-plane incident-field component of the p-polarized light to the coupled field; B/C, ratio of the contributions from the in-plane and perpendicular-to-the-plane incident-field components of the p-polarized light to the coupled field. The values are presented for different tip apex angles of the near-field probe.
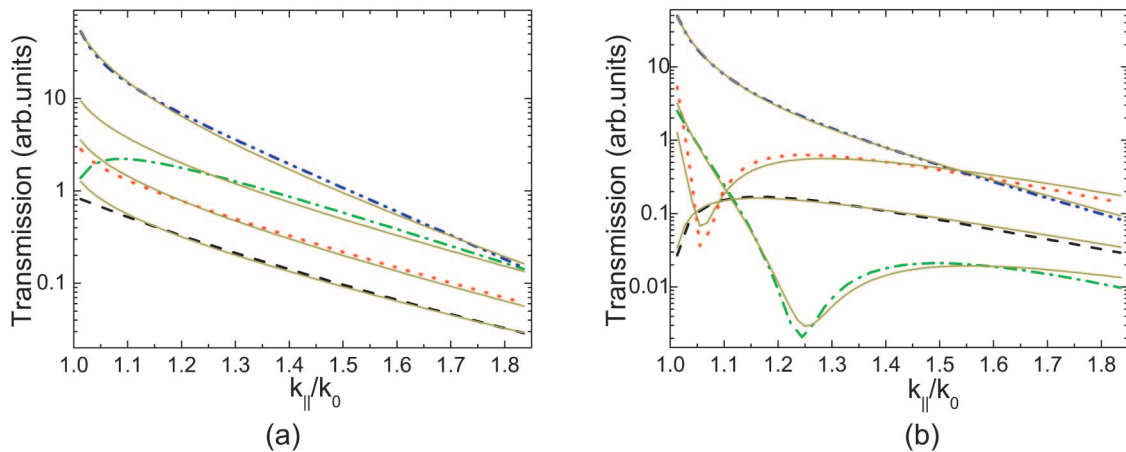
Fig. 7. (Color online) Evanescent field domain of numerical results shown in Fig. 6 along with the fitted (as explained in Section 5) curves shown with solid lines. Marking of the curves simulated for different apex angles is as in Fig. 6.

ization filtering is seen in the fact that the ratio B/C was found to be larger than 1.

The same fitting procedure has been carried out using the simulated data corresponding to the evanescent field components for all considered tip apex angles (Table 1). Here the agreement between exact (calculated) and approximated [Eqs. (6)] dependencies is seen to be rather good (Fig. 7). Use of the fitting parameters allows one to interpret the results of numerical simulations revealing their connections to the features observed experimentally. Thus the increase in the distance z_0 with the apex angle implies that sharper tips are better suited for SNOM imaging with high spatial resolution, which has been one of the first features associated with the PT-SNOM.[3–5] On the other hand, the increase in coefficients A and B with the apex angle means that the detected signal is expected to be larger for blunter tips, a feature that has also been frequently noted (e.g., Refs. 5 and 13). Note that the ratio B/C that is very large for sharp tips decreases rapidly with the increase in the apex angle, a tendency that agrees well with the experimental results on polarization filtering[22] and on detection of surface plasmon polaritons, whose electric field is predominantly polarized perpendicular to the surface.[23] Moreover, the fitting parameters obtained for the simulated (in 2D geometry) data (Table 1) are also consistent with those found when fitting the experimental signal dependencies measured with the fiber tip with an apex angle of $\approx 22°$ [Fig. 2(a)]. Finally, the phase difference ($\varphi \sim \pi$) between two contributions to the signal for p polarization can be accounted for partly with the phase difference between the corresponding field components, i.e., E_z and E_x, as was seen above, and partly with the phase difference in the dipole scattered radiation along and perpendicular to the incident field polarization. However, this explanation should be elaborated (which requires further investigations) to obtain a better understanding of the SNOM detection and its polarization properties.

Concluding this section, we comment on the non-monotonic behavior of simulated signal dependencies for p polarization and the apex angles of 30° and 50° [Fig. 7(b)]. It can be qualitatively understood in the following way. Coupling of the perpendicular (to the surface) field component (E_z) is less efficient than that of the parallel one (E_x), whereas, for low spatial frequencies $k_\parallel/k_0$ (≥ 1), the former is much stronger than the latter for p-polarized radiation as was seen above. When increasing the spatial frequency $k_\parallel/k_0$, the parallel component increases rapidly and, being detected more efficiently, comes into force. The transition from the signal that originated mainly from the perpendicular field component (E_z) to that related mainly to the parallel one (E_x) results in local minima in the transmission curves shown in Fig. 7(b) for the tip apex angles of 30° and 50°. Note that it remains to be seen to what extent this effect found here with 2D simulations would manifest itself in the experiments and accurate (3D) modeling.

6. Conclusion

Summarizing, we have considered the characterization of a near-field optical probe in terms of detection efficiency of different spatial frequencies paying special attention to the detection of evanescent field components. Experimental results as well as numerical simulations carried out in 2D geometry have been presented for the detection of both s and p polarization and found consistent. The detection roll-off for high spatial frequencies corresponding to the evanescent field components was both observed in the experiment and obtained during the simulations of the incident field. It has been further fitted using a simple expression for the transfer function, which was derived introducing an effective point of (dipolelike) detection inside the probe tip. We have found it possible to fit reasonably well both the experimental and the simulation data for evanescent field components, implying that the developed approximation of the near-field transfer function can serve as a simple, rational, and sufficiently reliable means of fiber probe characterization.

We believe that the results obtained serve as a better understanding of the SNOM imaging and can be used for treating experimentally obtained images, especially those containing significantly different spatial frequencies (e.g., corresponding to different scaling objects), by taking explicitly into account the dependence of detection efficiency on the spatial frequency [see Eqs. (5) and (6)]. In principle, by measuring the detected signal at one spatial frequency (corresponding to the evanescent illumination), one should be able to predict fairly accurately the level of the signal at other (higher) spatial frequencies and, e.g., determine the attainable spatial resolution for a given noise level. The relatively simple expressions that we derived can also be further elaborated, serving as the first approximation so that the very shape of the fiber tip apex (e.g., the tip radius) would be taken into account.

References

1. J. W. Goodman, *Introduction to Fourier Optics* (McGraw-Hill, 1996).
2. J. C. Weeber, F. de Fornel, and J. P. Goudonnet, "Numerical study of the tip-sample interaction in the photon scanning tunneling microscope," Opt. Commun. **126,** 285–292 (1996).
3. D. P. Tsai, Z. Wang, and M. Moskovits, "Estimating the effective optical aperture of a tapered fiber probe in PSTM imaging," in *Scanning Probe Microscopies II,* C. C. Williams, ed., Proc. SPIE **1855,** 93–104 (1993).
4. A. J. Meixner, M. A. Bopp, and G. Tarrack, "Direct measurement of standing evanescent waves with a photon-scanning tunneling microscope," Appl. Opt. **33,** 7995–8000 (1994).
5. D. Van Labeke and D. Barchiesi, "Probes for scanning tunneling optical microscopy: a theoretical comparison," J. Opt. Soc. Am. A **10,** 2193–2201 (1993).
6. R. Carminati and J.-J. Greffet, "2-Dimensional numerical-simulation of the photon scanning tunneling microscope—concept of transfer-function," Opt. Commun. **116,** 316–321 (1995).
7. J. C. Weeber, E. Bourillot, A. Dereux, J. P. Goudonnet, Y. Chen, and C. Girard, "Observation of light confinement effects with a near-field optical microscope," Phys. Rev. Lett. **77,** 5332–5335 (1996).
8. J. R. Krenn, A. Dereux, J. C. Weeber, E. Bourillot, Y. Lacroute, J. P. Goudonnet, G. Schider, W. Gotschy, A. Leitner, F. R. Aussenegg, and C. Girard, "Squeezing the optical near-field zone by plasmon coupling of metallic nanoparticles," Phys. Rev. Lett. **82,** 2590–2593 (1999).
9. S. I. Bozhevolnyi and V. Coello, "Elastic scattering of surface plasmon polaritons: modeling and experiment," Phys. Rev. B **58,** 10899–10910 (1998).
10. A. G. Choo, H. E. Jackson, U. Thiel, G. N. De Brabander, and J. T. Boyd, "Near-field measurements of optical channel waveguides and directional-couplers," Appl. Phys. Lett. **65,** 947–949 (1994).
11. S. Bourzeix, J. M. Moison, F. Mignard, F. Barthe, A. C. Boccara, C. Licoppe, B. Mersali, M. Allovon, and A. Bruno, "Near-field optical imaging of light propagation in semiconductor waveguide structures," Appl. Phys. Lett. **73,** 1035–1037 (1998).
12. S. I. Bozhevolnyi, B. Vohnsen, E. A. Bozhevolnaya, and S. Berntsen, "Self-consistent model for photon scanning tunneling microscopy: implications for image formation and light scattering near a phase-conjugating mirror," J. Opt. Soc. Am. A **13,** 2381–2392 (1996).
13. B. Vohnsen and S. I. Bozhevolnyi, "Optical characterization of probes for photon scanning tunnelling microscopy," J. Microsc. (Oxford) **194,** 311–316 (1999).
14. S. I. Bozhevolnyi, B. Vohnsen, and E. A. Bozhevolnaya, "Transfer functions in collection scanning near-field optical microscopy," Opt. Commun. **172,** 171–179 (1999).
15. J.-J. Greffet and R. Carminati, "Image formation in near-field optics," Prog. Surf. Sci. **56,** 133–237 (1997).
16. L. Novotny, D. W. Pohl, and P. Regli, "Light propagation through nanometer-sized structures: the two-dimensional-aperture scanning near-field optical microscope," J. Opt. Soc. Am. A **11,** 1768–1779 (1994).
17. B. Hecht, H. Bielefeldt, D. W. Pohl, L. Novotny, and H. Heinzelmann, "Influence of detection conditions on near-field optical imaging," J. Appl. Phys. **84,** 5873–5882 (1998).
18. P. Bienstman and R. Baets, "Optical modelling of photonic crystals and VCSELs using eigenmode expansion and perfectly matched layers," Opt. Quantum Electron. **33,** 327–341 (2001).
19. N. Gregersen, B. Tromborg, V. S. Volkov, S. I. Bozhevolnyi, and J. Holm, "Topography characterization of a deep grating using near-field imaging," Appl. Opt. **45,** 117–121 (2006).
20. S. I. Bozhevolnyi, V. A. Markel, V. Coello, W. Kim, and V. M. Shalaev, "Direct observation of localized dipolar excitations on rough nanostructured surfaces," Phys. Rev. B **58,** 11441–11448 (1998).
21. A. Nesci, R. Dändliker, M. Salt, and H. P. Herzig, "Measuring amplitude and phase distribution of fields generated by gratings with sub-wavelength resolution," Opt. Commun. **205,** 229–238 (2002).
22. T. Grosjean and D. Courjon, "Polarization filtering induced by imaging systems: effect on image structure," Phys. Rev. E **67,** 046611 (2003).
23. S. I. Bozhevolnyi, "Localization phenomena in elastic surface-polariton scattering caused by surface roughness," Phys. Rev. B **54,** 8177–8185 (1996).